Science Advances
AAAS

Supplementary Materials for

Local Berry curvature signatures in dichroic angle-resolved photoelectron spectroscopy from two-dimensional materials

Michael Schüler*, Umberto De Giovannini, Hannes Hübener, Angel Rubio, Michael A. Sentef, Philipp Werner

*Corresponding author. Email: schuelem@stanford.edu

This PDF file includes:

Supplementary materials

Section S1. SOC effects in graphene and BiH

In this section we show that S_z is an approximate quantum number for the systems with SOC which we discuss in this work. To this end, we have solved the Kohn-Sham equations including the SOC (numerical details in the Materials and Methods section), treating the Bloch wave-functions $|\Psi_{\mathbf{k}\alpha}\rangle$ as general spinors. This allows for calculating the expectation value $S_z(\mathbf{k}) = \langle\Psi_{\mathbf{k}\alpha}|\hat{S}_z|\Psi_{\mathbf{k}\alpha}\rangle$, where $\hat{S}_z = (\hbar/2)\hat{\sigma}_z$ denotes the operator of the z-projection of the spin.
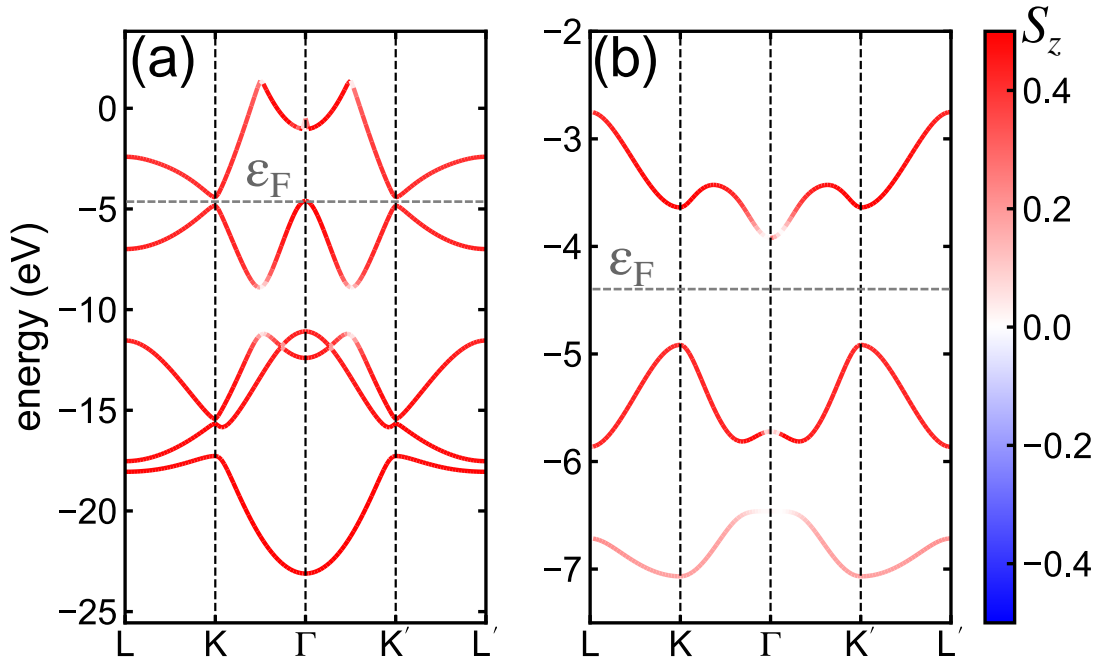
Fig. S1. Spin as quantum number. Spin expectation value $S(\mathbf{k})$ of the predominantly spin up bands for (a) graphene with enchanced SOC, and (b) BiH. The color bar is in units of $\hbar$.

Fig. S1 shows $S_z(\mathbf{k})$ for both graphene with enhanced SOC as well as for BiH with full intrinsic SOC. We have focused on the bands with predominant spin-up character close to the Fermi energy. As Fig. S1 demonstrates, $S_z(\mathbf{k})$ is very close to $+\hbar/2$ in the vicinity

of the K and K′ point for the top valence band and most parts of the bottom conduction band. Hence, S_z can be regarded as good quantum number, justifying the block-diagonal structure of the Hamiltonian Eq. (1) in the main text.

The physical explanation of why the SOC does not induce significant spin mixing is based on the restricted matrix elements with respect to the orbitals forming the top valence and bottom conduction band, respectively. The leading order of intrinsic SOC is the atomic contribution $\mathbf{L} \cdot \mathbf{S}$, computed on each sublattice site. The most important orbitals for the systems studied by us are s, p_z (forming a π band) and the p_x, p_y (forming σ bands) orbitals, respectivly. Evaluating $\mathbf{L} \cdot \mathbf{S}$ with respect to these atomic orbitals yields spin-mixing terms only for $\langle p_z | \mathbf{L} \cdot \mathbf{S} | p_x \rangle = -i\hat{S}_y$, $\langle p_z | \mathbf{L} \cdot \mathbf{S} | p_y \rangle = i\hat{S}_x$. Matrix elements with respect to p_x and p_y are proportional to $\hat{S}_z$, preserving S_z as quantum number. All other matrix elements vanish. Hence, noncollinear spin textures arise due to π–σ hybridization. For BiH, the σ orbital character dominates around the Dirac points [17], while the π–σ hybridization becomes active closer to the Γ-point and the lower valence band (see Fig. S1(b)). For graphene, on the other hand, the p_z orbitals dominate at the Dirac points; the atomic SOC vanishes. The π–σ hybridization gives rise to spin mixing closer to Γ in graphene (Fig. S1(a)). Hence, the next-nearest-neighbour SOC becomes the leading term for the π bands in the vicinity of the Dirac points (Kane-Mele term [45]). The Kane-Mele SOC is proportional to $\hat{S}_z$ as long as the lattice is completely planar.
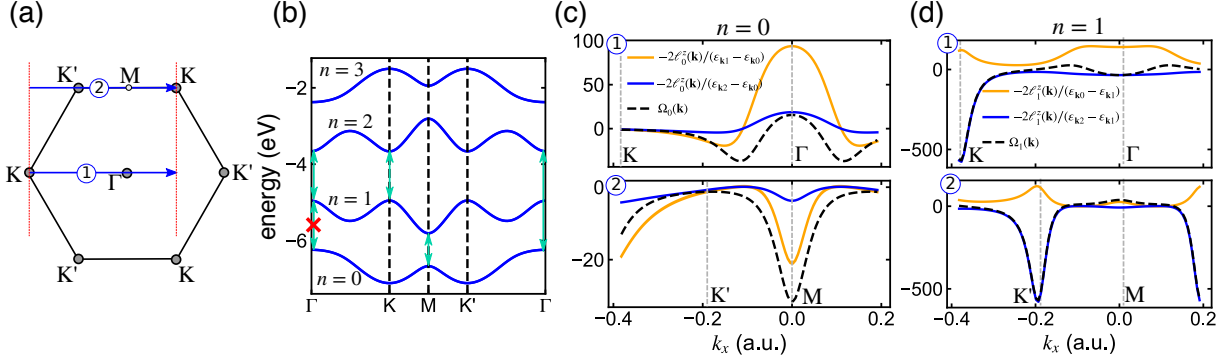
Fig. S2. Orbital polarization and Berry curvature of BiH. (a) Sketch of the Brillouin zone and the paths along high-symmetry points. (b) Band structure of BiH within the TB model with SOC. The arrows indicate hybridizations at the high-symmetry points important for the Berry curvature. (c), (d) Orbital polarization $\ell_n^z(\mathbf{k})$ and Berry curvature $\Omega_n(\mathbf{k})$ for the top two valence bands ($n = 0, 1$) along the paths indicated in (a). All quantities are shown for the spin-up channel.

Section S2. Orbital angular momentum and Berry curvature in multiband systems

As introduced in the main text, the z component of the orbital polarization for Bloch band n is defined by

$$\ell_n^z(\mathbf{k}) = \mathrm{Im}\langle \partial_{k_x} u_{\mathbf{k}n} | \hat{h}_\sigma(\mathbf{k}) - \varepsilon_{\mathbf{k}n} | \partial_{k_y} u_{\mathbf{k}n}\rangle \tag{1}$$

where $|u_{\mathbf{k}n}\rangle$ is the cell-periodic part. Replacing the derivatives in momentum space by the sum-of-states formula, one finds

$$\ell_n^z(\mathbf{k}) = \mathrm{Im} \sum_{n' \neq n} \frac{v_{nn'}^x(\mathbf{k}) v_{n'n}^y(\mathbf{k})}{\varepsilon_{\mathbf{k}n'} - \varepsilon_{\mathbf{k}n}} \tag{2}$$

where $v_{nn'}^x(\mathbf{k})$ ($v_{nn'}^y(\mathbf{k})$) is the velocity matrix element with respect to the x (y) direction. Comparing to the Kubo formula for the Berry curvature

$$\Omega_n(\mathbf{k}) = -2\,\mathrm{Im} \sum_{n' \neq n} \frac{v_{nn'}^x(\mathbf{k}) v_{n'n}^y(\mathbf{k})}{(\varepsilon_{\mathbf{k}n'} - \varepsilon_{\mathbf{k}n})^2} \tag{3}$$

one realizes that both quantities are tightly connected. In case there is only one hybridization gap between bands n and n' with sufficiently small energy difference $|\varepsilon_{\mathbf{k}n} - \varepsilon_{\mathbf{k}n'}|$ (for

instance, the top valence (v) and bottom conduction (c) band), while all other energy differences are larger, one finds

$$\ell_n^z(\mathbf{k}) \approx -\frac{1}{2}(\varepsilon_{\mathbf{k}n'} - \varepsilon_{\mathbf{k}n})\Omega_n(\mathbf{k}) \ , \quad \Omega_n(\mathbf{k}) \approx -\frac{2\ell_n^z(\mathbf{k})}{\varepsilon_{\mathbf{k}n'} - \varepsilon_{\mathbf{k}n}} \tag{4}$$

Considering a fixed band n, the band with the dominant hybridization n' can change over the Brillouin zone, which makes the evaluation of the Berry curvature via the relation (4) difficult. However, assuming the band structure and the orbital character at the hybridization points in the Brillouin zone are known, one can obtain a good guess for the involved bands and still extract information on the Berry curvature from Eq. (4). We demonstrate this idea for BiH, which is a four-band system within the TB model.

Let us consider the lowest band ($n = 0$ in Fig. S2(b)). At Γ, we would expect that $n' = 1$ is the largest constribution to the sum in Eq. (3). Inspecting Fig. S2(c) (upper panel), we see that around Γ Eq. (4) is fulfilled for $n' = 2$ instead. This is due to the dipole-forbidden transition, which is indicated by the red cross in Fig. S2(b). Away from Γ, the multiband nature becomes apparent, as $\Omega_0(\mathbf{k})$ changes sign; as $-2\ell_0^z(\mathbf{k})/(\varepsilon_{\mathbf{k}2} - \varepsilon_{\mathbf{k}0})$ is positive along this path, this shows that $n' = 1$ plays a certain role. Inspecting the M point, there is only the contribution $n' = 1$ which can have large weight due to the smaller gap. Indeed, the Berry curvature estimated by Eq. (4) agrees well with the actual Berry curvature, even along the considered path.

In the main text, we present the photoemission spectra for the top valence band $n = 1$. Here, the topological properties are dominated by the behavior around the K and K$'$ point, respectively. Following path 1 (Fig. S2(d)), we find that $\Omega_1(\mathbf{k})$ is almost identical to the estimate (4), especially at the hight-symmetry points K and Γ. The only slight difference is that $\Omega_1(\mathbf{k})$ changes sign away from Γ, which indicates some influence of the transition $(n = 1) \leftrightarrow (n = 0)$. This is expected from the small energy difference between band $n = 0$

and $n = 1$ in the Γ-K direction (Fig. S2(b)).

Similarly, we can follow path 2 passing through K$'$ and M. Again, the Berry curvature and the estimate (4) are matching perfectly. The only exception is the M point. This is consistent with the gap $\varepsilon_{\mathrm{M1}} - \varepsilon_{\mathrm{M0}}$ being smaller than $\varepsilon_{\mathrm{M2}} - \varepsilon_{\mathrm{M1}}$. Thus, inserting $n' = 0$ into Eq. (4) still allows for an accurate estimate of the Berry curvature.

This analysis demonstrates that the circular dichroism from the top valence band presented in the main text is indeed dominated by the Berry curvature at K and K$'$, respectively. More generally, knowing the band structure allows for guessing which terms in Eq. (3) are predominant (at each $\mathbf{k}$ separately). This works particularly well for high-symmetry points, where also the orbital character of the corresponding bands is known from symmetry considerations. Combining these ingredients, the orbital polarization $\ell_n^z(\mathbf{k})$ – which determines the circular dichroism – provides insights in the Berry curvature via the estimate Eq. (4) even for multiband systems.

Section S3. Wave-packet picture

To understand the self-rotation and the associated orbital magnetic moment, we employ the wave packet picture. Let us consider a wave packet with respect to band α of the form

$$W_{\mathbf{k}\alpha}(\mathbf{r}) = \int d\mathbf{q}\, a(\mathbf{k}, \mathbf{q}) \psi_{\mathbf{q}\alpha}(\mathbf{r}) = \int d\mathbf{q}\, a(\mathbf{k}, \mathbf{q}) e^{i\mathbf{q}\cdot\mathbf{r}} u_{\mathbf{q}\alpha}(\mathbf{r}) \tag{5}$$

For computing ARPES matrix elements, it is convenient to introduce an analogue of cell-periodic functions by $F_{\mathbf{k}\alpha}(\mathbf{r}) = e^{-i\mathbf{k}\cdot\mathbf{r}} W_{\mathbf{k}\alpha}(\mathbf{r})$. The envelope function $a(\mathbf{k}, \mathbf{q})$ represents a narrow distribution around a central wave vector $\mathbf{k}$; its precise functional form does not play a role. Denoting the center of the wave packet by

$$\mathbf{r}_c = \langle W_{\mathbf{k}\alpha}|\mathbf{r}|W_{\mathbf{k}\alpha}\rangle = \langle F_{\mathbf{k}\alpha}|\mathbf{r}|F_{\mathbf{k}\alpha}\rangle \tag{6}$$

one defines [30] the angular momentum as

$$\langle \hat{\mathbf{L}} \rangle = \langle W_{\mathbf{k}\alpha} | (\mathbf{r} - \mathbf{r}_c) \times \hat{\mathbf{p}} | W_{\mathbf{k}\alpha} \rangle = \langle F_{\mathbf{k}\alpha} | (\mathbf{r} - \mathbf{r}_c) \times \hat{\mathbf{p}} | F_{\mathbf{k}\alpha} \rangle \tag{7}$$

where $\hat{\mathbf{p}}$ denotes the momentum operator. The wave packet representation of OAM (7) naturally leads to the so-called modern theory of magnetization [30] in the limit of $a(\mathbf{k}, \mathbf{q}) \to \delta(\mathbf{q} - \mathbf{k})$.

Expansion in eigenfunctions of angular momentum

To quantify the OAM, we expand the wave packet $F_{\mathbf{k}\alpha}(\mathbf{r})$ onto eigenfunctions of the OAM $\hat{L}_z$

$$F_{\mathbf{k}\alpha}(\mathbf{r}) = \frac{1}{\sqrt{2\pi}} \sum_m \mathcal{F}_{\mathbf{k}\alpha,m}(s, z) e^{im\theta} \tag{8}$$

Here, θ is the angle measured in the 2D plane, taking $\mathbf{r}_c$ as the origin, while $s = |\mathbf{r}_\| - \mathbf{r}_c|$ is the corresponding distance. Inserting the expansion (8) into Eq. (7) yields the simple expression

$$\begin{aligned} \langle \hat{L}_z \rangle &= \sum_m m \int_0^\infty ds\, s \int_{-\infty}^\infty dz\, |\mathcal{F}_{\mathbf{k}\alpha,m}(s, z)|^2 \\ &\equiv \sum_m m P_{\mathbf{k}\alpha}(m) \end{aligned} \tag{9}$$

Hence, a nonzero orbital angular momentum projection in the z direction can be associated with an imbalance of the occupation of angular momentum states $P_{\mathbf{k}\alpha}(m)$.

Photoemission matrix elements

Approximating the initial Bloch states $|\psi_{\mathbf{k}\alpha}\rangle$ by the wave packet state $|W_{\mathbf{k}\alpha}\rangle$ and the final states by plane waves, the dipole matrix elements are given by

$$\begin{aligned} M_\alpha^{(\pm)}(\mathbf{p}, p_\perp) &= \int d\mathbf{r}_\| \int_{-\infty}^\infty dz\, e^{-i\mathbf{p}\cdot\mathbf{r}_\|} e^{-ip_\perp z} (x \pm iy) W_{\mathbf{k}\alpha}(\mathbf{r}) \\ &= \frac{1}{\sqrt{2}} \int d\mathbf{r}_\| \int_{-\infty}^\infty dz\, e^{-i(\mathbf{p}-\mathbf{k})\cdot\mathbf{r}_\|} e^{-ip_\perp z} (x \pm iy) F_{\mathbf{k}\alpha}(\mathbf{r}) \end{aligned} \tag{10}$$

Now we insert the angular-momentum representation (8) and the plane-wave expansion around $\mathbf{r}_c$

$$e^{\mathrm{i}(\mathbf{p}-\mathbf{k})\cdot\mathbf{r}_\parallel} = e^{\mathrm{i}(\mathbf{p}-\mathbf{k})\cdot\mathbf{r}_c}\sum_m \mathrm{i}^m J_m(|\mathbf{p}-\mathbf{k}|s)e^{\mathrm{i}m(\theta-\theta(\mathbf{p},\mathbf{k}))}$$

where $\theta(\mathbf{p},\mathbf{k})$ is the angle defining the direction of $\mathbf{p}_\parallel - \mathbf{k}$, into Eq. (10). Thus, we can express the matrix elements as

$$M_\alpha^{(\pm)}(\mathbf{p},p_\perp) = e^{\mathrm{i}(\mathbf{p}-\mathbf{k})\cdot\mathbf{r}_c}\sum_m (-\mathrm{i})^{m\pm 1}e^{\mathrm{i}(m\pm 1)\theta(\mathbf{p},\mathbf{k})}$$
$$\times \int_0^\infty ds \int_{-\infty}^\infty dz\, e^{-\mathrm{i}p_\perp z} J_{m\pm 1}(|\mathbf{p}-\mathbf{k}|s)s^2 \mathcal{F}_{\mathbf{k}\alpha,m}(s,z) \qquad (11)$$

Assuming the distribution $a(\mathbf{k},\mathbf{q})$ to be sufficiently narrow, such that Bloch states are recovered, the energy conservation implies $\mathbf{p} \approx \mathbf{k}$. As $J_m(x) \to 0$ for $x \to 0$ with $m \neq 0$, only the term with $m = 0$ contributes to the sum in Eq. (11). The dominant matrix element simplifies to

$$M_\alpha^{(\pm)}(\mathbf{k},p_\perp) = \int_0^\infty ds \int_{-\infty}^\infty dz\, e^{-\mathrm{i}p_\perp z} s^2 \mathcal{F}_{\mathbf{k}\alpha,\mp 1}(s,z) \qquad (12)$$

This expression demonstrates that the asymmetry of OAM eigenstates with $m = \pm 1$ determine the circular dichroism.

Illustration for hBN

In order to illustrate the discussion above, we have constructed Bloch wave packets according to Eq. (5), choosing a distibution function $a(\mathbf{k},\mathbf{q}) = a_0 \exp[-(\mathbf{q}-\mathbf{k})^2/(2\Delta k^2)]$ (a_0 is a normalization constant). The underlying Bloch wave functions are constructed using the TB model for hBN.

We have computed the projection onto planar OAM eigenfunctions (Eq. (8)) and the corresponding weights $P_{\mathbf{k}\alpha}(m) =$ for the valence band ($\alpha = v$), as presented in Fig. S3.
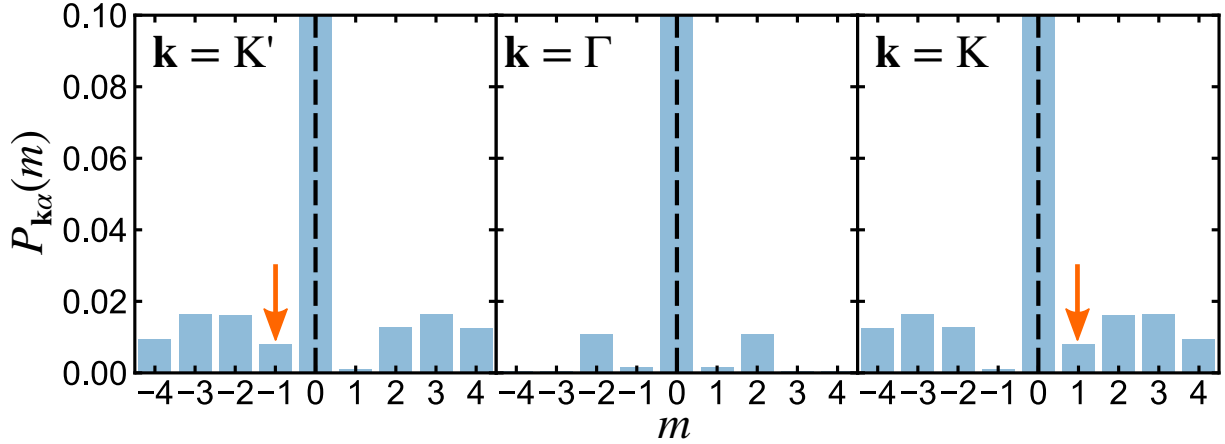
Fig. S3. Angular momentum in hBN. Weights of the projections onto OAM eigenfunctions according to Eq. (8) for the TB model of hBN. The width of the distribution is $\Delta k = 0.025$ in reduced coordinates. The arrows indicate the dominant contribution for the matrix elements (12).

As Fig. S3 demonstrates, the OAM eigenstate $m = -1$ ($m = +1$) dominates at $\mathbf{k} = \mathrm{K}'$ ($\mathbf{k} = \mathrm{K}$). At $\mathbf{k} = \mathrm{K}'$, we expect photoelectrons emitted by RCP light – this is in line with Fig. (3) in the main text. The behavior at $\mathbf{k} = \mathrm{K}$ is reversed. In contrast, at $\mathbf{k} = \Gamma$ the weights are symmetric. Hence, vanishing dichroism is expected around the Γ-point; we have confirmed this behavior by explicitly calculating the circular dichroism within the full TB+PW model.

Section S4. TB modeling of photoemission

We used the tight-binding (TB) representation of the Bloch states as described in the Materials and Methods section. In this section we present the details on how photoemission spectra are computed in the TB+PW model. For completeness, let us recapitulate the TB representation of the Bloch states

$$\psi_{\mathbf{k}\alpha}(\mathbf{r}) = \frac{1}{\sqrt{N}} \sum_{\mathbf{R}} e^{i\mathbf{k}\cdot\mathbf{R}} \phi_{\mathbf{k}\alpha}(\mathbf{r} - \mathbf{R}) = \frac{1}{\sqrt{N}} \sum_{\mathbf{R}} \sum_{j} C_{\alpha j}(\mathbf{k}) e^{i\mathbf{k}\cdot(\mathbf{R}+\mathbf{t}_j)} w_j(\mathbf{r} - \mathbf{R}) \tag{13}$$

Here, we are employing the convention where the phase factor $e^{i\mathbf{k}\cdot\mathbf{t}_j}$ ($\mathbf{t}_j$ denotes the sub-lattice site positions). The TB orbitals are approximated as

$$w_j^\gamma(\mathbf{r}) = C_j \mathbf{u}_\gamma \cdot (\mathbf{r} - \mathbf{t})_j \exp\left[-\alpha_j(\mathbf{r} - \mathbf{t}_j)^2\right] \tag{14}$$

where $\mathbf{u}_\gamma$ is the unit vector in the direction $\gamma = x, y, z$. The parameters C_j and α_j are fitted to atomic orbitals.

Matrix elements

To further simplify the analysis, we approximate the final states as plane-waves (PW). The cell-periodic part $\tilde{\chi}_{\mathbf{p},p_\perp}(\mathbf{r}) = e^{-i\mathbf{k}\cdot\mathbf{r}}\chi_{\mathbf{p},p_\perp}(\mathbf{r})$ thus reduces to $\tilde{\chi}_{\mathbf{p},p_\perp}(\mathbf{r}) = N^{-1/2}e^{ip_\perp z}$, where N is the normalization as in the Wannier representation (13).

Due to the periodicity of both the initial and final states, the matrix element entering Fermi's Golden rule

$$M_\alpha(\mathbf{p}, p_\perp) = \langle \chi_{\mathbf{p},p_\perp} | \hat{\epsilon} \cdot \mathbf{r} | \psi_{\mathbf{k}\alpha} \rangle \tag{15}$$

is only nonzero if $\mathbf{p} = \mathbf{k} + \mathbf{G}$, where $\mathbf{G}$ is a reciprocal lattice vector. Here, we focus on ARPES from the first BZ, so that $\mathbf{G} = 0$.

To evaluate the photoemission matrix element in the length gauge, we employ the identity

$$\mathbf{r}\psi_{\mathbf{k}\alpha}(\mathbf{r}) = ie^{i\mathbf{k}\cdot\mathbf{r}}\nabla_\mathbf{k} u_{\mathbf{k}\alpha}(\mathbf{r}) - i\nabla_\mathbf{k}\psi_{\mathbf{k}\alpha}(\mathbf{r})$$

which transforms the dipole operator into a cell-periodic expression. Inserting the Wannier

representation (Eq. (7) in the main text) into Eq. (15), we find for the matrix elements

$$
\begin{aligned}
M_\alpha(\mathbf{k}, p_\perp) &= \frac{\mathrm{i}}{\sqrt{N}} \sum_\mathbf{R} \int \mathrm{d}\mathbf{r}\, \tilde{\chi}^*_{\mathbf{k}p_\perp}(\mathbf{r}) \hat{\epsilon} \cdot \nabla_\mathbf{k} \left[e^{-\mathrm{i}\mathbf{k}\cdot(\mathbf{r}-\mathbf{R})} \phi_{\mathbf{k}\alpha}(\mathbf{r}-\mathbf{R}) \right] \\
&\quad - \frac{\mathrm{i}}{N} \sum_\mathbf{R} \int \mathrm{d}\mathbf{r}\, \chi^*_{\mathbf{k}p_\perp}(\mathbf{r}) \hat{\epsilon} \cdot \nabla_\mathbf{k} \left[e^{\mathrm{i}\mathbf{k}\cdot\mathbf{R}} \phi_{\mathbf{k}\alpha}(\mathbf{r}-\mathbf{R}) \right] \\
&= \sqrt{N} \int \mathrm{d}\mathbf{r}\, \chi^*_{\mathbf{k}p_\perp}(\mathbf{r}) \hat{\epsilon} \cdot \mathbf{r} \phi_{\mathbf{k}\alpha}(\mathbf{r}) - \frac{1}{\sqrt{N}} \sum_\mathbf{R} \hat{\epsilon} \cdot \mathbf{R} \int \mathrm{d}\mathbf{r}\, \chi^*_{\mathbf{k}p_\perp}(\mathbf{r}) \phi_{\mathbf{k}\alpha}(\mathbf{r}) \quad (16)
\end{aligned}
$$

The second term in Eq. (16) vanishes.

Note that the origin $\mathbf{r}_0$ from which the dipole is measured ($\mathbf{r} \to \mathbf{r} - \mathbf{r}_0$) is arbitrary if exact scattering states $|\chi_{\mathbf{p},p_\perp}\rangle$ are used. However, within the PW approximation, the initial and final states are not exactly orthogonal, which results in a slight dependence on $\mathbf{r}_0$. Here, we consistently choose $\mathbf{r}_0 = (\mathbf{t}_B - \mathbf{t}_A)/2$, where $j = A, B$ denotes the sublattice sites. This choice encodes as many symmetries as possible and leads to a very good agreement of the ARPES intensity between TDDFT and the TB approach.

Defining the Fourier transformed Wannier orbitals by

$$
\varphi_j(\mathbf{k}, p_\perp) = \int \mathrm{d}\mathbf{r}\, e^{-\mathrm{i}\mathbf{k}\cdot\mathbf{r}} e^{-\mathrm{i}p_\perp z} w_j(\mathbf{r}) \quad (17)
$$

the matrix elements can be expressed via

$$
M_\alpha(\mathbf{k}, p_\perp) = \mathrm{i} \sum_j C_{\alpha j}(\mathbf{k}) e^{\mathrm{i}\mathbf{k}\cdot\mathbf{t}_j} \hat{\epsilon} \cdot \left[\mathrm{i}\nabla_\mathbf{k} - \mathbf{r}_0 \right] \varphi_j(\mathbf{k}, p_\perp) \quad (18)
$$

Section S5. Pseudospin picture

In this appendix we demonstrate that the circular dichroism for π-conjugate systems like graphene and hBN is directly related to the orbital pseudospin. This provides a clear link to a topological phase transition, which is characterized by a sign change of the pseudospin in the BZ.

The starting point is the expression (18) for the matrix element in the length gauge. The Fourier transformation of the Wannier orbital centered around $\mathbf{t}_j$ can be conveniently expressed as $\varphi_j(\mathbf{k}, p_\perp) = e^{-i\mathbf{k}\cdot\mathbf{t}_j}\widetilde{\varphi}_j(\mathbf{k}, p_\perp)$. In particular, if the Wannier orbital $w_j(\mathbf{r})$ is radially symmetric around $\mathbf{t}_j$ and symmetric or antisymmetric along the z-axis, $\widetilde{\varphi}_j(\mathbf{k}, p_\perp)$ becomes a purely real or imaginary function. Simplifying Eq. (18) in this way, we obtain

$$M_\alpha(\mathbf{k}, p_\perp) = \hat{\epsilon} \cdot \sum_j C_{\alpha j}(\mathbf{k})(\mathbf{t}_j - \mathbf{r}_0 + i\nabla_{\mathbf{k}})\widetilde{\varphi}_j(\mathbf{k}, p_\perp)$$

The difference of the modulus squared matrix elements upon inserting $\hat{\epsilon}^{(\pm)}$ yields

$$\begin{aligned}
\Delta\mathcal{M}_\alpha(\mathbf{k}, p_\perp) &\equiv \left|M_\alpha^{(+)}(\mathbf{k}, p_\perp)\right|^2 - \left|M_\alpha^{(-)}(\mathbf{k}, p_\perp)\right|^2 \\
&= 2\mathrm{Im}\sum_{j,l} C_{\alpha j}(\mathbf{k})C_{\alpha l}^*(\mathbf{k})\left[[(\mathbf{t}_j - \mathbf{r}_0)\widetilde{\varphi}_j(\mathbf{k}, p_\perp) + i\nabla_{\mathbf{k}}\widetilde{\varphi}_j(\mathbf{k}, p_\perp)]\right. \\
&\quad \left.\times [(\mathbf{t}_l - \mathbf{r}_0)\widetilde{\varphi}_l^*(\mathbf{k}, p_\perp) - i\nabla_{\mathbf{k}}\widetilde{\varphi}_l^*(\mathbf{k}, p_\perp)]\right]
\end{aligned} \tag{19}$$

where we take the z component of the vector product. Further evaluating Eq. (19), the matrix element asymmetry can be decomposed into two terms

$$\Delta\mathcal{M}_\alpha(\mathbf{k}, p_\perp) = \Delta\mathcal{M}_\alpha^{(1)}(\mathbf{k}, p_\perp) + \Delta\mathcal{M}_\alpha^{(1)}(\mathbf{k}, p_\perp) \tag{20}$$

where

$$\Delta\mathcal{M}_\alpha^{(1)}(\mathbf{k}, p_\perp) = 2\mathrm{Re}\sum_{j,l} C_{\alpha j}(\mathbf{k})C_{\alpha l}^*(\mathbf{k})\Big[(\mathbf{t}_l - \mathbf{r}_0)\widetilde{\varphi}_l^*(\mathbf{k}, p_\perp) \times \nabla_{\mathbf{k}}\widetilde{\varphi}_j(\mathbf{k}, p_\perp) \tag{21}$$

$$+ (\mathbf{t}_j - \mathbf{r}_0)\widetilde{\varphi}_j(\mathbf{k}, p_\perp) \times \nabla_{\mathbf{k}}\widetilde{\varphi}_l^*(\mathbf{k}, p_\perp)\Big] \tag{22}$$

and

$$\Delta\mathcal{M}_\alpha^{(2)}(\mathbf{k}, p_\perp) = 2\mathrm{Im}\sum_{j,l} C_{\alpha j}(\mathbf{k})C_{\alpha l}^*(\mathbf{k})\nabla_{\mathbf{k}}\widetilde{\varphi}_j(\mathbf{k}, p_\perp) \times \nabla_{\mathbf{k}}\widetilde{\varphi}_l^*(\mathbf{k}, p_\perp) \tag{23}$$

Both the contributions (21) and (23) are important. However, assuming a radial symmetry of the Wannier orbitals around their center renders $\widetilde{\varphi}_j(\mathbf{k}, p_\perp)$ real and, furthermore, $\widetilde{\varphi}_j(\mathbf{k}, p_\perp) = \widetilde{\varphi}_j(k, p_\perp)$. In this case, $\Delta\mathcal{M}_\alpha^{(2)}(\mathbf{k}, p_\perp) = 0$.

Let us now specialize to the two-band TB model of graphene or hBN. The atomic p_z orbitals fulfill the above requirement. Thus, we arrive at

$$\Delta\mathcal{M}_\alpha^{(1)}(\mathbf{k}, p_\perp) = \frac{4}{k} \sum_{j,l} \mathrm{Re}\left[C_{\alpha j}(\mathbf{k})C_{\alpha l}^*(\mathbf{k})\right]$$
$$\cdot\left((\mathbf{t}_l - \mathbf{r}_0) \times \mathbf{k}\right)\widetilde{\varphi}_j(k, p_\perp)\widetilde{\varphi}_l'(k, p_\perp)$$

Here, $\nabla_\mathbf{k}\widetilde{\varphi}_j(k, p_\perp) = (\mathbf{k}/k)\widetilde{\varphi}_j'(k, p_\perp)$ has been exploited. Furthermore, the sublattice sites $j = \mathrm{A}, \mathrm{B}$ are equivalent, such that $\widetilde{\varphi}_j(k, p_\perp) = \widetilde{\varphi}(k, p_\perp)$. Inserting $\mathbf{r}_0 = (\mathbf{t}_B - \mathbf{t}_A)/2$ and $\mathbf{t}_A = 0$, $\mathbf{t}_B = \boldsymbol{\tau}$, the asymmetry simplifies to

$$\Delta\mathcal{M}_\alpha^{(1)}(\mathbf{k}, p_\perp) = \frac{2}{k}\left(|C_{\alpha A}(\mathbf{k})|^2 - |C_{\alpha B}(\mathbf{k})|^2\right)[\mathbf{k} \cdot \boldsymbol{\tau}]_z$$
$$\times \widetilde{\varphi}(k, p_\perp)\widetilde{\varphi}'(k, p_\perp) \tag{24}$$

Eq. (24) contains an important message: the difference of the sublattice site occupation, or, in other words, the pseudospin

$$\sigma_z(\mathbf{k}) = |C_{\alpha A}(\mathbf{k})|^2 - |C_{\alpha B}(\mathbf{k})|^2 \tag{25}$$

determines the sign of the dichroism in each valley. For graphene, one finds $\sigma_z(\mathbf{k}) = 0$ and hence no circular dichroism is expected.

Furthermore, a topological phase transition can be detected based on Eq. (24). To support this statement, let us express the generic two-band Hamiltonian by

$$\hat{h}(\mathbf{k}) = \mathbf{D}(\mathbf{k}) \cdot \hat{\boldsymbol{\sigma}} \tag{26}$$

The main difference between a topologically trivial and nontrival system is the zero crossing of the $D_z(\mathbf{k})$ component. The states (spin-up or spin-down) correspond to sublattice sites; the Pauli matrices represent pseudospin operators. Suppose that the second state (spin-down) possesses a lower energy (like in hBN, where the nitrogen lattice site has a

deeper potential), corresponding to $D_z(\mathbf{k}) < 0$. The eigenstate of the Hamiltonian (26) then reads

$$\mathbf{C}(\mathbf{k}) = \frac{1}{\mathcal{N}} \begin{pmatrix} D_z(\mathbf{k}) - |\mathbf{D}(\mathbf{k})| \\ -D_x(\mathbf{k}) + iD_y(\mathbf{k}) \end{pmatrix} \tag{27}$$

Evaluating the pseudospin in the z-direction yields

$$\sigma_z(\mathbf{k}) = \frac{2}{\mathcal{N}} D_z(\mathbf{k}) \left(|\mathbf{D}(\mathbf{k})| - D_z(\mathbf{k}) \right) < 0$$

Trivial case— Assuming $D_z(\mathbf{k}) < 0$ across the whole BZ (which yields a trivial band insulator) then leads to *opposite* dichroism at K and K′. This is a direct consequence of TRS: $\sigma_z(\mathbf{k}) = \sigma_z(-\mathbf{k})$. Thus, we find

$$\int_{V_1} d\mathbf{k}\, \Delta\mathcal{M}_\alpha^{(1)}(\mathbf{k}, p_\perp) = - \int_{V_2} d\mathbf{k}\, \Delta\mathcal{M}_\alpha^{(1)}(\mathbf{k}, p_\perp) \tag{28}$$

Here, the BZ is divided equally into two parts V_1 and V_2, with V_1 (V_2) containing K (K′).

Topologically nontrivial case— In contrast, a topologically nontrivial phase is chacterized by $D_z(\mathbf{k}) > 0$ in some part of the BZ. One can show that the eigenvector in the vicinity of K′ has to be chosen as

$$\mathbf{C}(\mathbf{k}) = \frac{1}{\mathcal{N}} \begin{pmatrix} D_z(\mathbf{k}) + |\mathbf{D}(\mathbf{k})| \\ D_x(\mathbf{k}) + iD_y(\mathbf{k}) \end{pmatrix} \tag{29}$$

which results in

$$\sigma_z(\mathbf{k}) = \frac{2}{\mathcal{N}} D_z(\mathbf{k}) \left(|\mathbf{D}(\mathbf{k})| + D_z(\mathbf{k}) \right) > 0$$

For this reason, the pseudospin $\sigma_z(\mathbf{k})$ is has the *same* sign at both K and K′. Therefore, this behavior is reflected in the matrix element asymmtry (24), and thus the relation (28) breaks.
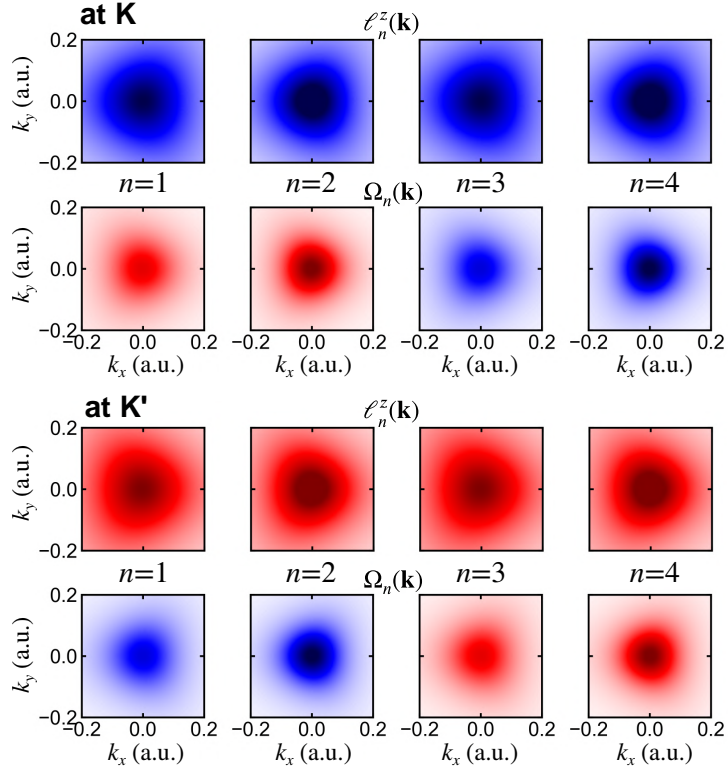
Fig. S4. Topological properties of monolayer TMDCs. Figure S4: Orbital polarization (upper rows) and Berry curvature (lower rows) of monolayer TMDCs at the valleys K and K′. We adopted the parameters for WSe2. The color scale is normalized to the maximum absolute value, ranging from blue (negative values) to red (positive values). Results are shown for the spin-up channel. Momenta are measured relative to K and K′, respectively.

Hence, the following simple criterion can be formulated: if the valley-integrated circular dichroism has the *same* sign at K and K′, the system represents a Chern insulator. This conclusion is supported by the *ab initio* calculations for graphene with enhanced SOC and the discussion of the Haldane model in the main text.

Section S6. Orbital polarization for monolayers TMDC

To show that the direct connection between orbital polarization and Berry curvature holds for important materials beyond those considered in our work, we discuss monolayer

transition metal dichalcogenides (TMDCs) of the type MX_2. Close to the Γ point and the K and K' valleys, respectively, the multiband problem reduces to an effective description involving two bands with SOC. The effective Hamiltonian can be obtained by $\mathbf{k} \cdot \mathbf{p}$ perturbation theory, expanding the *ab initio* tight-binding Hamiltonian for MoS_2, $MoSe_2$, WS_2 and WSe_2, as detailed in Ref. [29].

Based on the $\mathbf{k} \cdot \mathbf{p}$ Hamiltonian, we have computed the orbital angular momentum $\ell_n^z(\mathbf{k})$ and the Berry curvature $\Omega_n(\mathbf{k})$ for the four bands $n = 1, \ldots, 4$ in the vicinity of the K/K' valleys (Fig. S4). For concreteness, we have used the parameters for WSe_2 [29]. Due to the reflection symmetry, $\hat{S}_z$ is an approximate quantum number (exact quantum number within the lowest-order $\mathbf{k} \cdot \mathbf{p}$ theory) close to the valleys; the main effect of the SOC is an effective Zeemann splitting.

In Fig. S4 we present $\ell_n^z(\mathbf{k})$ and $\Omega_n(\mathbf{k})$ at the respective valleys. As Fig. S4 shows, both quantities are proportional to each other. For valence bands, $\ell_n^z(\mathbf{k})$ and $\Omega_n(\mathbf{k})$ have opposite sign, while they possess the same sign for conduction bands. This is exactly as expected from Eq. (4). The overall trivial topological character is reflected in the sign change that $\ell_n^z(\mathbf{k})$ and $\Omega_n(\mathbf{k})$ undergoes upon replacing K$\leftrightarrow$K'. Hence, the circular dichroism due to the pronounced valley polarization $\ell_n^z(\mathbf{k})$ is due to the properties of the Berry curvature.

On the level of the $\mathbf{k} \cdot \mathbf{p}$ Hamiltonian, the one-to-one correspondence between Berry curvature and orbital polarization (4) becomes exact. This implies that Eq. (4) is still a good estimate even beyond the $\mathbf{k} \cdot \mathbf{p}$ approximation. We remark that similar considerations apply to the Γ point.

Furthermore, a similar $\mathbf{k} \cdot \mathbf{p}$ treatment applies for $2H$ bilayers of the above materials. Therefore, the connection between orbital polarization and Berry curvature remains well defined at the high-symmetry points.